







The fates of the circumgalactic medium in the FIRE simulations

Zachary Hafen ¹★, Claude-André Faucher-Giguère ¹, Daniel Anglés-Alcázar,^{2,3}
Jonathan Stern ¹, Dušan Kereš,⁴ Clarke Esmerian,⁵ Andrew Wetzel ⁶,
Kareem El-Badry ⁷, T. K. Chan ^{4,8} and Norman Murray⁹†

¹Department of Physics and Astronomy and Center for Interdisciplinary Exploration and Research in Astrophysics (CIERA), Northwestern University, 2145 Sheridan Road, Evanston, IL 60208, USA

²Center for Computational Astrophysics, Flatiron Institute, 162 Fifth Avenue, New York, NY 10010, USA

³Department of Physics, University of Connecticut, 196 Auditorium Road, U-3046, Storrs, CT 06269-3046, USA

⁴Department of Physics, Center for Astrophysics and Space Sciences, University of California, San Diego, 9500 Gilman Drive, La Jolla, CA 9209, USA

⁵Department of Astronomy and Astrophysics, The University of Chicago, Chicago, IL 60637, USA

⁶Department of Physics, University of California, Davis, CA 95616, USA

⁷Department of Astronomy and Theoretical Astrophysics Center, University of California, Berkeley, CA 94720-3411, USA

⁸Institute for Computational Cosmology, Durham University, South Road, Durham DH1 3LE, UK

⁹Canadian Institute for Theoretical Astrophysics, University of Toronto, 60 St George Street, ON M5S 3H8, Canada

Accepted 2020 March 28. Received 2020 March 25; in original form 2019 October 3

ABSTRACT

We analyse the different fates of the circumgalactic medium (CGM) in FIRE-2 cosmological simulations, focusing on the redshifts $z = 0.25$ and 2 representative of recent surveys. Our analysis includes 21 zoom-in simulations covering the halo mass range $M_h(z=0) \sim 10^{10} - 10^{12} M_\odot$. We analyse both where the gas ends up after first leaving the CGM (its ‘proximate’ fate) and its location at $z = 0$ (its ‘ultimate’ fate). Of the CGM at $z = 2$, about half is found in the ISM or stars of the central galaxy by $z = 0$ in $M_h(z=2) \sim 5 \times 10^{11} M_\odot$ haloes, but most of the CGM in lower mass haloes ends up in the intergalactic medium (IGM). This is so even though most of the CGM in $M_h(z=2) \sim 5 \times 10^{10} M_\odot$ haloes first accretes on to the central galaxy before being ejected into the IGM. On the other hand, most of the CGM mass at $z = 0.25$ remains in the CGM by $z = 0$ at all halo masses analysed. Of the CGM gas that subsequently accretes on to the central galaxy in the progenitors of $M_h(z=0) \sim 10^{12} M_\odot$ haloes, most of it is cool ($T \sim 10^4$ K) at $z = 2$ but hot ($\sim T_{\text{vir}}$) at $z \sim 0.25$, consistent with the expected transition from cold mode to hot mode accretion. Despite the transition in accretion mode, at both $z = 0.25$ and 2 $\gtrsim 80$ per cent of the cool gas in $M_h \gtrsim 10^{11} M_\odot$ haloes will accrete on to a galaxy. We find that the metallicity of CGM gas is typically a poor predictor of both its proximate and ultimate fates. This is because there is in general little correlation between the origin of CGM gas and its fate owing to substantial mixing while in the CGM.

Key words: galaxies: formation – galaxies: evolution – galaxies: haloes – intergalactic medium – cosmology: theory.

1 INTRODUCTION

Both observations and simulations indicate that galaxies from dwarfs through galaxies in clusters are enclosed in enormous gaseous atmospheres (e.g. Steidel et al. 2010; Ford et al. 2013; Hummel et al. 2013; Bordoloi et al. 2014; Liang & Chen 2014; Stocke et al. 2014; Werk et al. 2014; Johnson et al. 2017). It has become clear in recent years that these gaseous atmospheres, also known as the circumgalactic medium (CGM), crucially affect the evolution

of galaxies. For example, the CGM mass can exceed that of the central galaxy (e.g. Tumlinson, Peebles & Werk 2017; Hafen et al. 2019). Moreover, the CGM mediates powerful interactions between galaxies and the larger scale intergalactic medium (IGM), such as cosmic inflows (e.g. Kereš et al. 2005; Dekel & Birnboim 2006; Prochaska & Wolfe 2009; Faucher-Giguère, Kereš & Ma 2011) and powerful galactic winds (e.g. Martin 2005; Veilleux, Cecil & Bland-Hawthorn 2005; Davé, Oppenheimer & Finlator 2011; Muratov et al. 2015; Anglés-Alcázar et al. 2017; Fielding et al. 2017).

The large gas mass present in the CGM, much of which is enriched with metals, raises the question of what happens to the CGM observed in different surveys, i.e. what are the different fates of the CGM? This a key question for the physical interpretation

* E-mail: zachary.h.hafen@gmail.com

† Canada Research Chair in Astrophysics.

of observational surveys of the CGM, at both low (e.g. Tumlinson et al. 2011; Bouché et al. 2013; Stocke et al. 2013; Bordoloi et al. 2014; Rubin et al. 2014; Johnson, Chen & Mulchaey 2015; Chen et al. 2018; Burchett et al. 2019) and high (e.g. Steidel et al. 2010; Rudie et al. 2012; Prochaska, Hennawi & Simcoe 2013) redshifts. The fates of the CGM, in particular, inform us about the whether circumgalactic gas primarily accretes on to galaxies, moves out in outflows that potentially enrich the IGM with metals, or remains in the CGM for cosmological time-scales. The fates of the CGM are also important for our understanding of different observed phenomena. Consider the massive CGM of low-redshift $\sim L^*$ galaxies, which have been the focus of comprehensive surveys with *HST/COS* (e.g. Werk et al. 2013; Johnson, Chen & Mulchaey 2015; Keeney et al. 2017). If this CGM remains as gaseous haloes until $z \approx 0$, then it may contribute to observed high-velocity clouds (e.g. Putman, Peek & Joungh 2012) or X-ray emitting gas (e.g. Henley & Shelton 2010; Henley et al. 2010; Gupta et al. 2012; Fang et al. 2015). On the other hand, if all the O VI-traced gas in L^* haloes accretes on to the central galaxy, then it could provide fuel for stars to form at a rate up to $\sim 1\text{--}10 \times$ the observed star formation rate (Mathews & Prochaska 2017; McQuinn & Werk 2018; Stern et al. 2018).

In this work, we trace the history of gas elements (commonly referred to as ‘particle tracking’) to study the different fates of the CGM in the FIRE cosmological zoom-in simulations (Hopki et al. 2014; Hopkins et al. 2018).¹ This paper complements our previous analysis of the origins of the CGM in the same simulations (Hafen et al. 2019, hereafter H19), as well as our analysis of the role of the cosmic baryon cycle in the build-up of central galaxies in FIRE (Anglés-Alcázar et al. 2017). The present analysis also complements several previous particle tracking studies in other simulations, which generally adopted a ‘galaxy-centric’ rather than a ‘CGM-centric’ perspective (e.g. Oppenheimer et al. 2010; van de Voort et al. 2011; Nelson et al. 2013; Ford et al. 2014; Christensen et al. 2018; Ho, Martin & Turner 2019; Tollet et al. 2019). The FIRE simulations simultaneously include the cosmological environment as well as the effects of galactic winds generated by energy injection on the scale of individual star-forming regions, making them well suited for predictions of the gas flows that occur in the CGM. In previous papers, we analysed other bulk properties of the CGM in the FIRE simulations (Muratov et al. 2015, 2017; Stewart et al. 2017; El-Badry et al. 2018; Ji et al. 2019) and have made predictions of its observability in absorption and emission (Faucher-Giguère et al. 2015, 2016; Srahan et al. 2016; van de Voort et al. 2016; Hafen et al. 2017).

Our analysis covers both the fate of gas immediately after it leaves the CGM (which we refer to as its *proximate fate*) and the fate of the gas by $z = 0$ (which we refer to as its *ultimate fate*). By studying the proximate fates of CGM gas, we address how CGM gas elements contribute to the baryon cycle in the near term. Our analysis of the ultimate fates of the CGM tells us where the gas ends up by $z = 0$. Analysing both the proximate and ultimate fates is important to gain insight into the baryon cycle because of the importance of recycling and ‘fall back’: gas that accretes on to a galaxy can later be ejected back into the CGM by galactic winds, while gas that ejected from haloes can later reaccrete on to the CGM. We focus on the CGM at $z = 0.25$ and 2, which are representative of major recent surveys referenced above.

The structure of this paper is as follows. In Section 2, we describe the simulations used and our particle tracking analysis methods. Our

main results are presented in Section 3, including the past and future locations of CGM gas (Section 3.1), trajectories of gas elements of different fates (Section 3.2), and how CGM fates depend on halo mass, temperature, and metallicity (Section 3.3). We also address the connection between the origin of a CGM gas element and its fate (Section 3.4). We discuss our results in Section 4 and conclude in Section 5.

Throughout, we assume a standard flat Λ CDM cosmology with $\Omega_m \approx 0.32$, $\Omega_\Lambda = 1 - \Omega_m$, $\Omega_b \approx 0.049$, and $H_0 \approx 67 \text{ km s}^{-1} \text{ Mpc}^{-1}$ (Planck Collaboration VI 2018).²

2 METHODS

2.1 Simulations

In this paper, we analyse 21 FIRE-2 cosmological hydrodynamic ‘zoom-in’ simulations generated with the multimethod gravity and hydrodynamics code `{\sc GIZMO}`³ (Hopkins 2015). The same simulations were previously analysed in H19, where they are described in more detail. The simulations were produced using `{\sc GIZMO}`’s meshless finite-mass (‘MFM’) solver. In this mode, there is no mass flux between hydrodynamic resolution elements and we can use the particles advected with the flow to track the history of gas parcels. The main haloes of our simulations span the mass range of $M_h(z=0) \sim 10^{10}\text{--}10^{12} M_\odot$. As in H19, for the sake of brevity we refer to main haloes with $M_h(z=0) \sim 10^{10}$, 10^{11} , and $10^{12} M_\odot$ simply as $10^{10} M_\odot$ progenitors, $10^{11} M_\odot$ progenitors, and $10^{12} M_\odot$ progenitors, respectively (these correspond to simulations whose name begins with m10, m11, or m12, respectively). We identify and track the evolution of dark matter haloes using the `{\sc Amiga Halo Finder}` (Gill, Knebe & Gibson 2004; Knollmann & Knebe 2009), and adopt the virial overdensity definition of Bryan & Norman (1998).

The physics implemented in the FIRE-2 simulations is described fully in Hopkins et al. (2018). We summarize some of the main elements here. The simulations include radiative heating and cooling processes over $T = 10\text{--}10^{10}$ K, including photoelectric heating, free–free emission, low-temperature cooling from molecules and fine-structure metal lines, Compton scattering with the cosmic microwave background, and high-temperature metal line cooling. We track nine metal species that dominate the cooling rate of cosmic gas, similar to Wiersma et al. (2009). Star particles are spawned when gas is self-gravitating, molecular, and has a density of at least $n_H = 1000 \text{ cm}^{-3}$. The star particles are treated as independent, simple stellar populations. The simulations include stellar feedback prescriptions for energy, momentum, mass, and metals from Type Ia and II supernovae and stellar winds, momentum from radiation pressure, and photoionization and photoelectric heating. Photoheating and photoionization account for both the cosmic UV background model (using the model of Faucher-Giguère et al. 2009) and approximations for local sources and self-shielding. The evolution of stellar populations, including the time-dependent feedback quantities, follows the `{\sc STARBURST99}` synthesis model (Leitherer et al. 1999) and assumes a Kroupa (2001) initial mass function.

²For consistency with previous work, some of our simulations were evolved with slightly different sets of cosmological parameters, but we do not expect this to significantly impact any of our results given the small differences in the parameters.

³<http://www.tapir.caltech.edu/~phopkins/Site/GIZMO.html>

¹FIRE project website: <https://fire.northwestern.edu/>.

Of the 21 simulations analysed in this work, 9 incorporate a subgrid model for metal diffusion between adjacent resolution elements. The purpose of the model is to capture subresolution-level metal mixing that is not by default accounted for by the MFM hydrodynamic solver, which does not capture mass flux between resolution elements. The primary assumption for the metal diffusion model is that the diffusion time-scale between elements scales with the eddy turnover time of the largest unresolved turbulent eddies, i.e. that unresolved turbulence exchanges metals between resolution elements. The details of our metal transport model are described in Hopkins (2017), Hopkins et al. (2018), and Escala et al. (2018).

2.2 Baryon cycle definitions

During the baryon cycle, baryons can be found in the IGM, the CGM, or galaxies. Baryons in galaxies can be either in the interstellar medium (ISM) or in stars. The definitions for galaxies and the CGM are the same as in H19. To summarize, for a given halo all gas within a radius R_{gal} and with $n_{\text{H}} > 0.13 \text{ cm}^{-3}$ is considered part of the central galaxy’s ISM and all stars within R_{gal} are considered part of that galaxy. We use $R_{\text{gal}} = 4R_{*,0.5}$, where $R_{*,0.5}$ is the stellar half-mass radius. For each halo, the CGM is defined as all the gas outside both the central galaxy and satellite galaxies, and in the case of the simulation’s main halo we further require that the CGM gas has $r > R_{\text{CGM, inner}}$ where $R_{\text{CGM, inner}} \equiv \max(1.2R_{\text{gal}}, 0.1R_{\text{vir}})$.⁴ This definition allows us to focus our analysis on CGM gas that is clearly separate from the main galaxy. The remaining main halo gas, i.e. gas within R_{gal} but $n_{\text{H}} < 0.13 \text{ cm}^{-3}$ and gas with $R_{\text{gal}} < r < R_{\text{CGM, inner}}$, is defined as the ‘galaxy–halo interface’. We define the IGM as gas outside the virial radii of all haloes in a simulation.

Zoom-in simulations simulate a single main halo at high resolution, and for each zoom-in we focus our analysis on the CGM of the main halo. We thus differentiate haloes that are satellites of the main halo and haloes external to the main halo. We do not distinguish the CGM of satellites from that of the main halo, given the extent to which they can mix through stripping and other processes. For the same reason, we only identify the galaxy–halo interface of the main galaxy, and not of satellite galaxies.

2.3 Proximate and ultimate fate classifications

The sample of particles tracked in this work is the same as in H19. Briefly, at both $z = 0.25$ and 2 we randomly sample 10^5 particles in the CGM of each main halo. We compile the full history of these particles at ~ 25 Myr time resolution, and use those histories to assign a proximate fate and an ultimate fate to each particle. Note that the proximate fate in general depends on the detailed history of a gas element, while the ultimate fate only depends on the final location of the gas.

The ultimate fate classification for a particle is simply the component of the baryon cycle the particle resides in at $z = 0$. This can be: the main galaxy’s CGM, the main galaxy, the galaxy–halo interface, a satellite galaxy, an external galaxy, the CGM of an external galaxy, or the IGM.

⁴In H19 we included satellite ISM as part of the CGM for the purpose of quantifying its mass contribution to the CGM. Having determined that satellite ISM is $\lesssim 5$ per cent of the CGM mass, we do not consider satellite ISM part of the CGM in this paper.

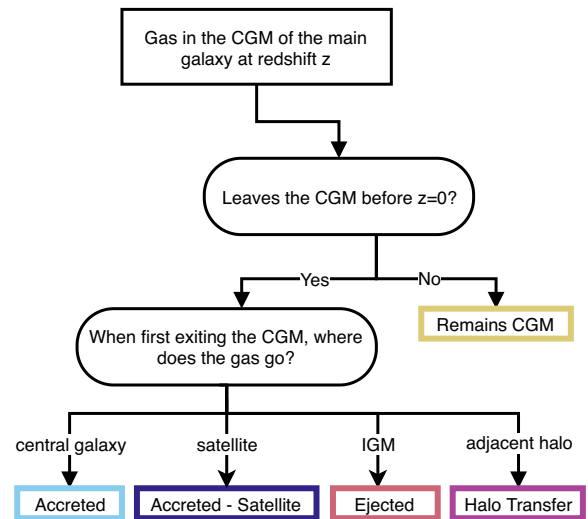


Figure 1. Flow chart summarizing how we classify the proximate fate of gas elements in the CGM of a galaxy. Gas is classified as *accreted* (on to the central galaxy), *accreted satellite* (accreted on to a satellite), *ejected* (into the IGM), or *halo transfer* depending on the component of the baryon cycle it transfers to upon leaving the CGM. Some gas stays continuously in the CGM until $z = 0$, i.e. it *remains CGM*.

The proximate fate of CGM gas identifies the next ‘component transition’ experienced. The main proximate fates are: accretion on to the central galaxy, accretion on to a satellite galaxy, ejection into the IGM, or continuous residence in the CGM until $z = 0$. Another possible proximate fate is ‘halo transfer’. Halo transfer occurs when gas is found within the halo of an external galaxy the snapshot after it was last in the CGM of the central galaxy. We have quantified halo transfer, but found that $\lesssim 1$ per cent of the CGM mass contributes to it, so we omit it from the figures in this paper for simplicity. Fig. 1 uses a flow chart to summarize how we assign proximate fates. Note that the proximate fates are insensitive to the time-scale on which gas leaves the CGM, with the exception of gas that remains in the CGM until $z = 0$.

Some care is needed to robustly identify when gas leaves the CGM. For example, gas that approaches the central galaxy but is blown away by a galactic wind before being incorporated in the galaxy can momentarily cross the (relatively large) R_{gal} radius. To avoid classifying such gas as accreted by the central galaxy, we only consider gas to have properly left the CGM if it is not contained by the galaxy–halo interface. Another means through which gas may spuriously appear to leave the CGM is through the momentary misidentification of the main halo by the halo finder. This causes the position of the main halo’s virial radius to change abruptly and can result in spuriously ‘ejected’ gas. To minimize this, we require that gas particles spend $t > 30$ Myr in a destination component to count as having left the CGM. Since the spacing between simulation snapshots is ~ 25 Myr, this requires that gas particles spend ≥ 2 snapshots in the destination component (there are some more finely spaced snapshots at very high redshift).

3 RESULTS

3.1 Past and future locations of CGM gas

Fig. 2 shows the results of identifying gas in the CGM at $z = 0.25$ or 2, and tracking the fraction of that mass residing in different

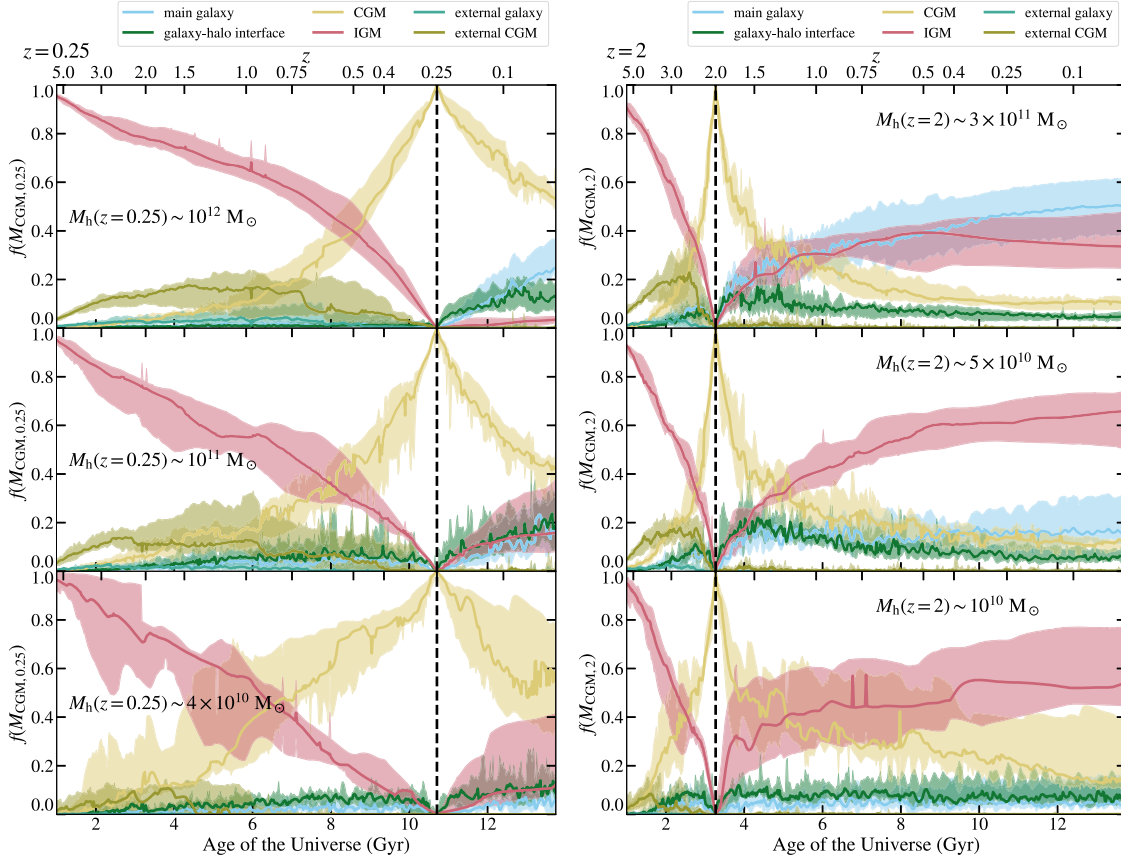


Figure 2. Fraction of mass in a given component of the baryon cycle as a function of time for gas that was/will be in the CGM at $z = 0.25$ (left) and $z = 2$ (right). We show gas in the main galaxy (blue), the galaxy–halo interface of the main galaxy (green), the CGM of the main galaxy (yellow), the IGM outside R_{vir} of any galaxy (red), within a galaxy other than the main galaxy (teal), and within the CGM of a galaxy other than the main galaxy (dark yellow). The solid line shows the median across different haloes in a given mass bin, and the shaded regions indicate the 16th–84th percentiles between haloes. Across the halo mass range analysed, both the build-up and the subsequent loss of half of the CGM mass occur over ~ 3 Gyr for $z = 0.25$ CGM gas and $\lesssim 1$ Gyr for $z = 2$ CGM gas.

components of the baryon cycle at subsequent and prior redshifts. The fractions at $z = 0$ correspond to ultimate fates, which we also study as a function of halo mass in Section 3.3.1.

As mentioned in the introduction, several CGM surveys in the last decade have targeted $z \sim 0.25$ using the Cosmic Origins Spectrograph on *HST* or $z \sim 2$ using 10 m-class ground-based observatories. As indicated by the yellow curves in the left-hand panels of Fig. 2, the fraction of $z = 0.25$ CGM gas that was in the CGM of the same galaxy at $z = 2$ is on average $\lesssim 10$ per cent for all halo masses included in our analysis. Thus, our simulations indicate that CGM surveys at different redshifts primarily probe different gas.

Of the CGM at $z = 2$, about half ends up in the central galaxy by $z = 0$ in $10^{12} M_{\odot}$ progenitor haloes; of the rest most is ejected into the IGM. Most of the CGM of lower mass haloes at $z = 2$ is ejected into the IGM over time. Interestingly, this is so even though most of the CGM in $M_{\text{h}}(z = 2) \sim 5 \times 10^{10} M_{\odot}$ haloes first accretes on to the central galaxy before being ejected into the IGM, as implied by our analysis of proximate fates in Section 3.3.1. This highlights the complex dynamics of inflows and outflows in the CGM, and in particular the fact that much of the gas accreted by galaxies can later be ejected in powerful winds, especially in low-mass haloes (e.g. Anglés-Alcázar et al. 2017). On the other hand, a significant

fraction of the CGM mass at $z = 0.25$ remains in the CGM by $z = 0$ at all halo masses analysed.

Up to ~ 20 per cent of the CGM mass at a given redshift spends time in haloes other than the main halo prior to accreting on to the main CGM. Of this mass, the vast majority is in the CGM of other haloes (as opposed to in external galaxies; see the dark yellow curves in Fig. 2). This external gas ends up in the main halo either when the external halo is accreted on to the main halo or when it is expelled by the external halo and subsequently accretes on to the CGM of the main galaxy (see the bottom panel of fig. 8 of H19 for an example of this for a $10^{10} M_{\odot}$ progenitor). This latter channel is related to the ‘intergalactic transfer’ identified in FIRE-1 simulations by Anglés-Alcázar et al. (2017), but in this case it consists primarily of CGM-to-CGM transfer, rather than galaxy-to-galaxy transfer.

To quantify the transient nature of the CGM, we calculate the ‘half-life’ of CGM gas. We define τ_{post} as the time for half the CGM mass (at $z = 0.25$ or 2) to move out of the CGM. Similarly, we define τ_{pre} as the time that it took for half of the CGM at a given redshift to join the CGM. Note that we define the half-life by tracking *fixed* gas elements, which is in general different from the time needed for total CGM mass to change by a factor of ≈ 2 as the net result of transfers in and out. The results are shown in Fig. 3. We plot the halo dynamical

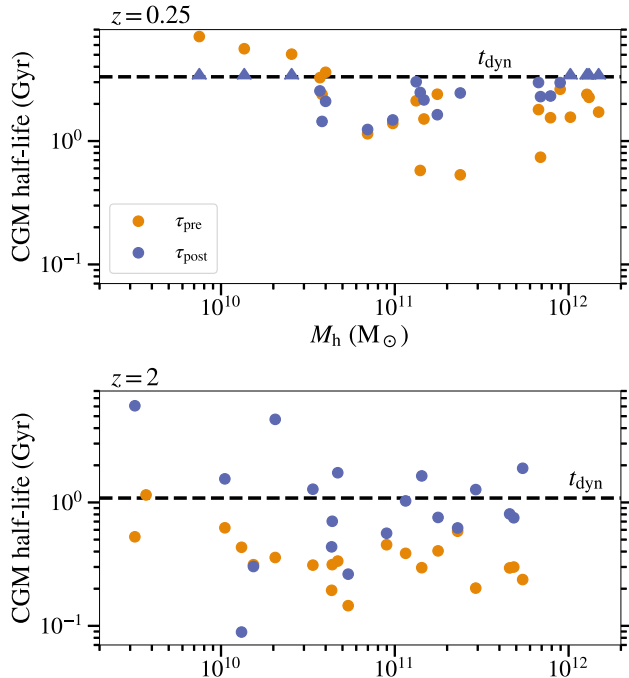


Figure 3. **Top:** The half-life of the CGM at $z = 0.25$. The ‘post’ half-life τ_{post} is defined as the time for half the CGM mass at $z = 0.25$ to move out of the CGM. Similarly, the ‘pre’ half-life τ_{pre} is defined as the time that it took for half of the CGM mass at $z = 0.25$ to join the CGM. Each point corresponds to a different halo. The arrows indicate lower limits on τ_{post} due to the fact that more than half the gas in the CGM at $z = 0.25$ is still in the CGM by $z = 0$. **Bottom:** Same but for $z = 2$. The half-life of CGM gas does not vary strongly with halo mass and has high halo-to-halo variability, especially at $z = 2$. For lower mass haloes, the CGM can consist of largely the same gas for multiple Gyr.

time $t_{\text{dyn}} \equiv 1/\sqrt{G\bar{\rho}}$ for comparison, where $\bar{\rho}$ is the mean density of the halo (recall that we define haloes using the redshift-dependent virial overdensity criterion from Bryan & Norman 1998). For some haloes at $z = 0.25$, the simulation ends before half the CGM mass transfers out, and for these haloes we indicate lower limits on τ_{post} (corresponding to the lookback time to $z = 0.25$) with upwards arrows. It is a coincidence that $t_{\text{lookback}}(z = 0.25) \approx t_{\text{dyn}}$, i.e. that the lower limits line up with the halo dynamical time at $z = 0.25$. The half-life is on average proportional to the halo dynamical time, but with $\gtrsim 1$ dex scatter. The exception is $M_{\text{h}} \lesssim 5 \times 10^{10} M_{\odot}$ haloes at $z = 0.25$, where heating by the cosmic UV background plays an important role in supporting the CGM.

3.2 Pathlines for different CGM fates

In this section, we analyse how the trajectories of particles found in the CGM of main haloes depend on their proximate and ultimate fates. The visualizations allow us to better understand the spatial distributions and physical behaviours of gas with different fates, and to illustrate how sightlines through haloes will in general include gas of different fates.

Fig. 4 shows the paths traced by 1000 randomly selected gas particles in the CGM of three representative simulations, one for each of our main halo mass bins. On the left, the paths are shown for 1 Gyr after $z = 0.25$ and on the right, for 0.5 Gyr after $z =$

2. The number of particles displayed for each proximate fate is proportional to the mass contribution of that fate to the CGM.⁵

Gas that will be accreted on to satellite galaxies closely follows the trajectory of satellite galaxies. Gas accreted on to satellites can be subsequently ejected from satellite galaxies. As apparent in some of the panels of Fig. 4 (e.g. for m12i at $z = 0$), some of the gas diverges from satellites after having been accreted by a satellite galaxy, indicating an outflow from the satellite. We discuss this more in Section 3.4, where we show that the primary origin of gas whose proximate fate is to be accreted on to a satellite is satellite wind. This reflects that fact that (relatively low-mass) star-forming satellite galaxies generally drive multiple episodes of gas ejection and recycling (see also Anglés-Alcázar et al. 2017).

As expected, gas whose proximate fate is to be accreted on to the central galaxy is preferentially found close to the central galaxy. Gas that will be ejected into the IGM appears to have quite diverse spatial distributions. In some cases gas that will accrete on to the central galaxy appears to block outflowing gas (e.g. m12i and m11q at $z = 2$). Interestingly, the $M_{\text{h}}(z = 0) \sim 10^{12} M_{\odot}$ halo shown in Fig. 4 contains very little gas at $z = 0.25$ that will be ejected into the IGM. This is consistent with the general finding in the FIRE simulations that galactic winds essentially disappear at low redshift in $\sim L^*$ galaxies (e.g. Muratov et al. 2015; Anglés-Alcázar et al. 2017; Stern et al. in prep.).

Fig. 5 shows radial distance from the centre of the halo versus time for particles found in the CGM at $z = 2$ in our example $10^{12} M_{\odot}$ progenitor, m12i. Equivalent plots for characteristic 10^{11} and $10^{10} M_{\odot}$ progenitors are found in Appendix A. We visualize five particles in each ultimate fate panel. Within each panel, the lines are coloured according to proximate fate. The particles visualized here were selected to illustrate the different proximate fates and a wide variety of trajectories possible for a given ultimate fate. Consistent with the bursty outflows in FIRE, gas that ends up in the central galaxy frequently recycles across all halo masses included in our analysis.

3.3 Fates of the CGM

3.3.1 Fate by halo mass

The left side of Fig. 6 shows the fraction of CGM mass with different proximate fates at $z = 0.25$ and 2. The right side shows the same but for different ultimate fates. The points are for individual haloes and the lines connect the medians between each halo mass bin. We highlight below some important trends regarding the possible fates of the CGM, as well as conclusions that can be drawn by comparing proximate and ultimate fates.

One evident difference in Fig. 6 between $z = 0.25$ and 2 is that while, overall, the most common proximate fate for CGM gas at $z = 0.25$ is to remain in the CGM until $z = 0$, only a tiny fraction $\sim 10^{-4}$ – 10^{-2} of the $z = 2$ CGM mass remains continuously in the CGM until the present time. Several factors contribute to this difference: (i) there is more time for gas to leave the CGM between $z = 2$ and 0; (ii) characteristic halo dynamical time-scales are shorter at $z = 2$; and (iii) in the case of the more massive $M_{\text{h}}(z = 0) \sim$

⁵Visualizations of the same simulations were presented for CGM origins in H19. However, in that study 500 gas particles were selected for each origin (independent of the origin’s mass contribution CGM). The visualizations shown in the present paper thus more faithfully represent the contributions of different processes to the total CGM mass.

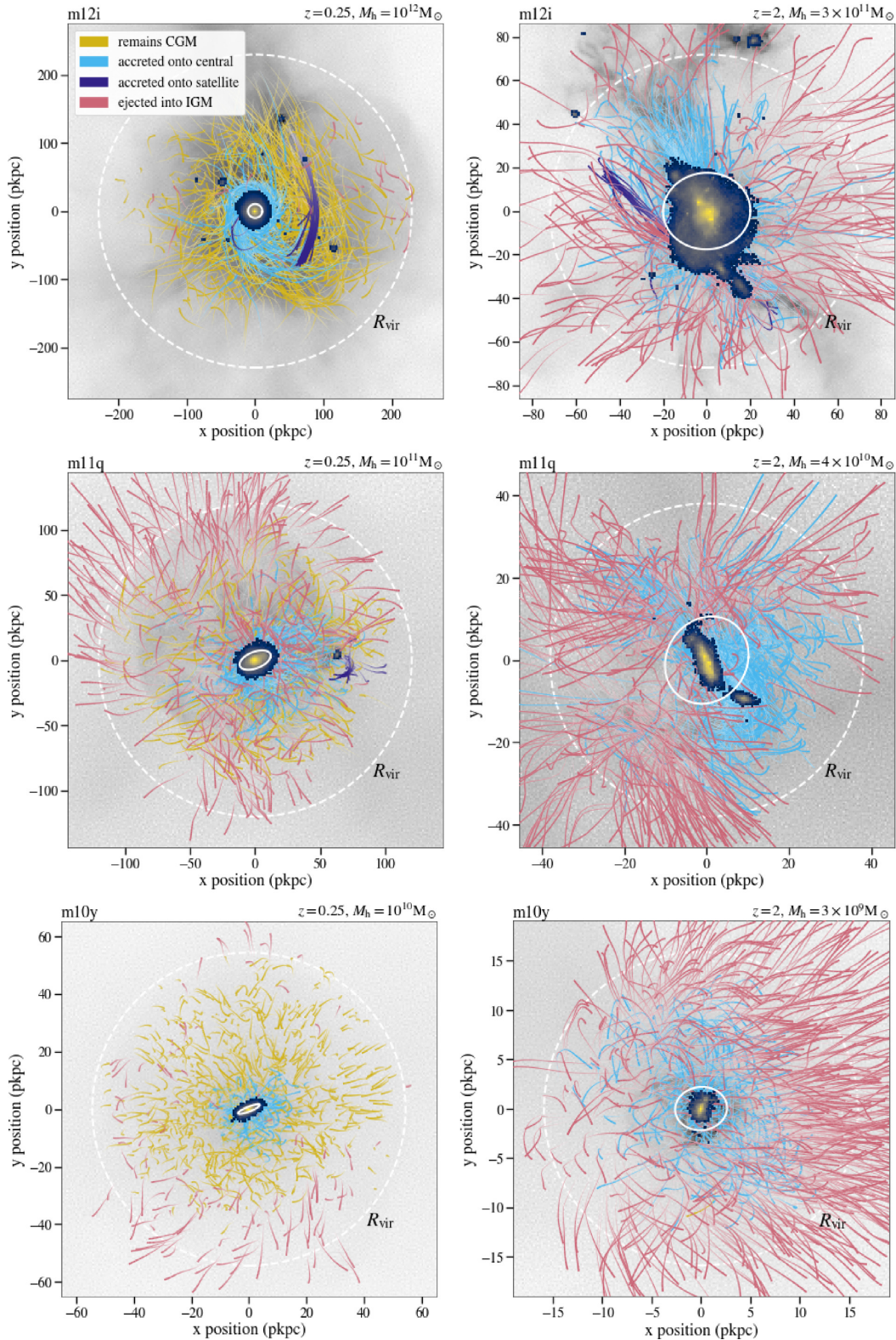


Figure 4. **Left:** Paths traced over the course of 1 Gyr by 1000 randomly selected particles in the CGM of m12i (top), m11q (centre), and m10y (bottom). Pathlines start at $z = 0.25$ and are coloured according proximate fate (i.e. the fate of gas immediately after it leaves the CGM). Lines become thicker with increasing time. The stellar mass surface density is plotted as a blue–yellow histogram. **Right:** Same as left, but for $z = 2$. To account for shorter halo dynamical times at this cosmic time, particle trajectories are plotted over the course of 0.5 Gyr, as opposed to 1 Gyr. In each panel, the virial radius of the main galaxy is plotted as a dashed white circle, and a circle with radius R_{gal} is centred on the main galaxies. The galaxy circle is rotated such that its plane is normal to the total angular momentum of the galaxy’s stars, indicating the orientation of the galactic disc. At $z = 2$ in the $\gtrsim 10^{11} M_{\odot}$ progenitors (m12i and m11q) gas that will be ejected into the IGM is often spatially separated from gas that will accrete on to the central galaxy, indicating that accreting gas can shape the paths of outflows.

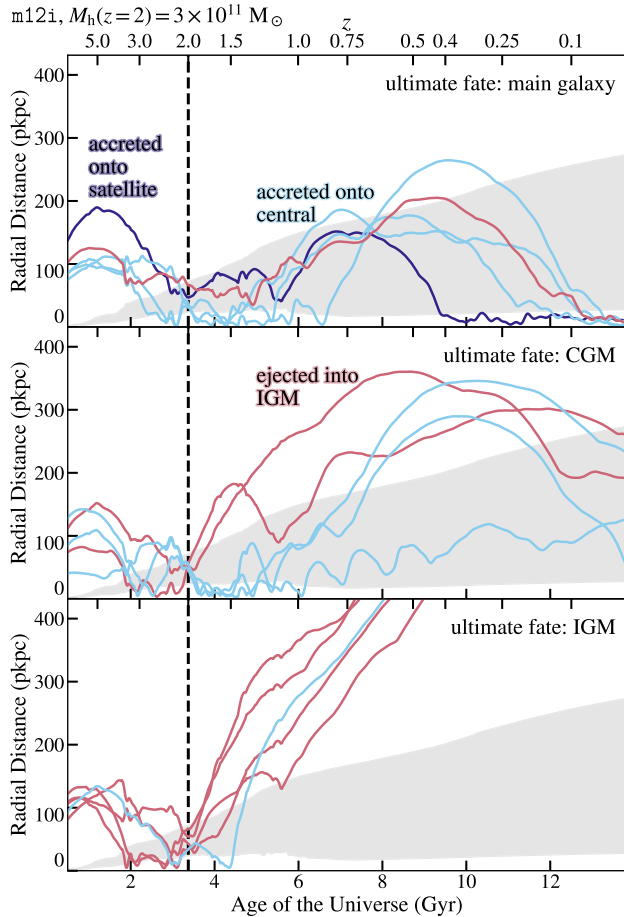


Figure 5. Distance from the central galaxy (in proper kpc) versus age of the universe for particles located in the CGM of $m12i$ at $z = 2$, a halo with $M_h(z = 2) = 3 \times 10^{11} M_\odot$. The grey shaded region shows the boundaries of the CGM. A vertical dashed line displays $z = 2$. Each panel corresponds to the location of the gas at $z = 0$ (its ultimate fate), with five particles per panel. Gas that will eventually be part of the central galaxy, the CGM of the main halo, and the IGM are the top, middle, and bottom panels, respectively. The colour of the gas particle indicates its proximate fate: gas accreted on to the main galaxy, on to satellites, or ejected into the IGM is coloured blue, purple, and red, respectively. Gas with a given ultimate fate can reach its destination through a wide variety of possible trajectories.

$10^{12} M_\odot$ progenitors at $z = 0.25$, the CGM forms a hot, pressure-supported atmosphere where accretion occurs on a cooling time, which is longer than the dynamical time (H19; Stern et al. 2019, 2020). The very small ‘remains CGM’ proximate fate fractions at $z = 2$, however, do not imply that there is essentially no gas in common between the CGM of galaxies at $z = 2$ and $z \sim 0$. Indeed, Fig. 6 shows that ~ 10 per cent of the $z = 2$ CGM is also in the CGM of the main galaxy at $z = 0$. To reconcile these results, we conclude that while almost all the $z = 2$ CGM leaves the CGM at least once by $z = 0$, a significant fraction *returns* to the CGM by $z = 0$. Gas accreted by galaxies can return to the CGM via galactic winds, while gas ejected into the IGM can later fall back on to the CGM.

Accretion on to the central galaxy is a common proximate fate for much of the CGM across the halo mass and redshift ranges analysed. On average, the prevalence of this proximate fate increases with halo mass and redshift. For $M_h(z = 0) \sim 10^{12} M_\odot$ progenitors at $z = 2$, corresponding to observed Lyman break galaxies (LBGs; e.g. Adelberger et al. 2005, albeit at the low-mass end), $\gtrsim 50$ per cent

of the CGM mass has this proximate fate. Moreover, the simulations indicate that up to ~ 80 per cent of the CGM of LBGs ends up in central galaxies by $z = 0$ (ultimate fate). The increasing fraction of the CGM mass that ends up in central galaxies (at both $z = 0.25$ and 2) is in agreement with the increasing efficiency with which observations imply that haloes convert their baryon budget into stars (e.g. Behroozi, Wechsler & Conroy 2013; Moster, Naab & White 2013).

The thin lines in the left column of Fig. 6 show CGM metal mass fractions with different proximate fates. The most significant differences between the proximate fates of the overall CGM mass versus the CGM metals are in the fractions of the mass/metals that will remain in the CGM versus will be accreted on to the central galaxy. In particular, the figure shows that metal-enriched gas is preferentially accreted relative to the overall CGM mass. In our sample, the vast majority of CGM metals originate in galactic winds (see H19, Fig. 10). The results thus imply that, at $z = 0.25$, CGM mass previously contributed by winds is more likely to reaccrete on to the central galaxy than other CGM mass (e.g. from IGM accretion). This effect is due both to the fact that the CGM mass fraction from previous winds is enhanced in the inner halo (Fig. 14 in H19) and to enhanced cooling of metal-rich gas (which tends to be overdense in addition to metal rich; Esmerian et al., in prep.). Fig. 6 shows that at $z = 2$ metallicity does not affect the relative fraction of accreting total gas mass versus metals, which is due in at least part to the almost complete absence of $z = 2$ CGM gas that remains continuously in the CGM until $z = 0$.

As discussed in Section 2.1, a subset of our simulations includes a subgrid prescription for metal diffusion that allows metals to diffuse between adjacent resolution elements.⁶ We use both simulations produced with and without subgrid metal diffusion to calculate the fractions in Fig. 6. This effectively assumes that the fates of CGM mass and metals are not significantly affected by subgrid metal diffusion. To check this assumption we calculated the CGM fractions with different proximate fates separately for simulations with and without metal diffusion, and found no differences that could not be explained by halo-to-halo variations and the small number of haloes. However, we caution that our simulation sample is relatively small, so significant differences could be revealed in a larger sample.

Overall, the accretion of CGM gas on to satellite galaxies is a subdominant proximate fate. However, this process becomes increasingly important with increasing halo mass, at both $z = 0.25$ and 2, and can be the proximate fate of up to ~ 10 per cent of the CGM mass in $10^{12} M_\odot$ haloes.

Concerning the ejection of gas into the IGM, Fig. 6 shows that this is the dominant ultimate fate of the $z = 2$ CGM of most of the haloes included in our analysis – the exception being the more massive $M_h(z = 0) \sim 10^{12} M_\odot$ progenitors, for which the simulations instead predict that most of the CGM ends up in the central galaxy. Ejection into the IGM is a dominant fate even though the proximate fate results show that most of the CGM in $M_h(z = 2) \sim 5 \times 10^{10} M_\odot$ haloes first accretes on to the central galaxy before being ejected into the IGM. This difference between proximate and ultimate fates again highlights the complex dynamics of the baryonic cycle.

⁶Technically, a metallicity scalar field is diffused but there is no actual transfer of mass between MFM resolution elements.

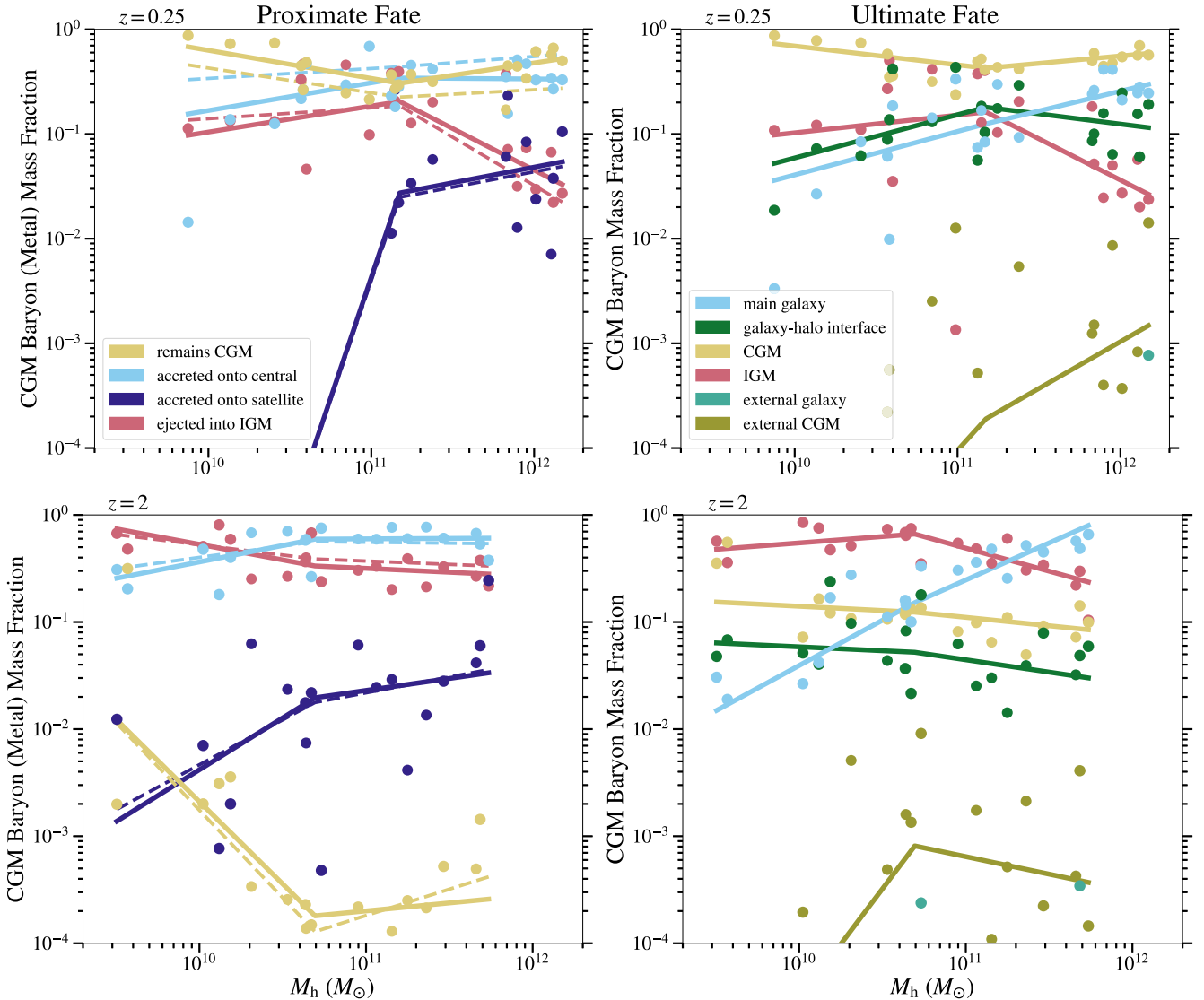


Figure 6. **Left:** Fraction of the total CGM baryon mass at $z = 0.25$ (top) or $z = 2$ (bottom) for different proximate fates (i.e. the component of the baryon cycle the gas transfers to upon leaving the CGM). Each point is a value from a simulation. The thick lines connect the medians for each mass bin. The thin dashed lines are calculated similarly, but for the fraction of CGM *metal* mass with different proximate fates, for which the raw data are not shown here. **Right:** Similar but for fractions with different ultimate fates. Similar but for the fraction of the total CGM baryon mass with different ultimate fates, i.e. the component of the baryon cycle where the gas ends up by $z = 0$.

3.3.2 Fates by temperature

Fig. 7 shows the temperature distributions of CGM gas of different proximate fates, for different halo mass bins. The solid lines indicate the median between haloes in a given halo mass bin, and the shaded regions indicate the 16th–84th percentile range. For each proximate fate, the log T probability distribution function (PDF) is weighted by the fraction of mass contributed to the CGM. Thus, an integral over log T corresponds to the fraction of the total CGM mass contributed by a given proximate fate. At a given temperature, the relative heights of the PDFs indicate the relative contribution of different proximate fates to CGM gas mass in a $\Delta \log T$ temperature interval.

One striking result in Fig. 7 is that, at $z = 2$, most of the CGM in the haloes analysed is cool, with $T \ll T_{\text{vir}}$ [$T_{\text{vir}} = GM_{\text{h}}\mu m_{\text{p}}/(2k_{\text{B}}R_{\text{vir}})$ is the halo virial temperature, where $\mu = 0.6$ is the assumed mean

molecular weight, m_{p} is the proton mass, and k_{B} is the Boltzmann constant]. Of this cool gas, most of it will next accrete on to the central galaxy in the progenitors of $\sim 10^{11}$ – $10^{12} M_{\odot}$ haloes. This is consistent with the importance of cold mode galactic accretion for these high-redshift haloes (e.g. Birnboim & Dekel 2003; Kereš et al. 2005, 2009). On the other hand, for the $M_{\text{h}} \sim 10^{12} M_{\odot}$ haloes at $z = 0.25$, we find that most of the CGM is hot with $T \sim T_{\text{vir}}$ and remains in the CGM until $z = 0$. Of the gas that accretes on to the central galaxy by $z = 0$, most of it is hot at $z = 0.25$, consistent with the development of hot mode accretion in the haloes of low-redshift $\sim L^*$ galaxies. We note that this may underestimate the amount of hot mode accretion, as the CGM gas that is cool already at $z = 0.25$ may previously have been shocked heated, i.e. it may have already cooled out of the hot halo.

Focusing on the fate of cool gas with $T \approx 10^4$ K, Fig. 7 implies that (to the extent that the present simulations are realistic), most

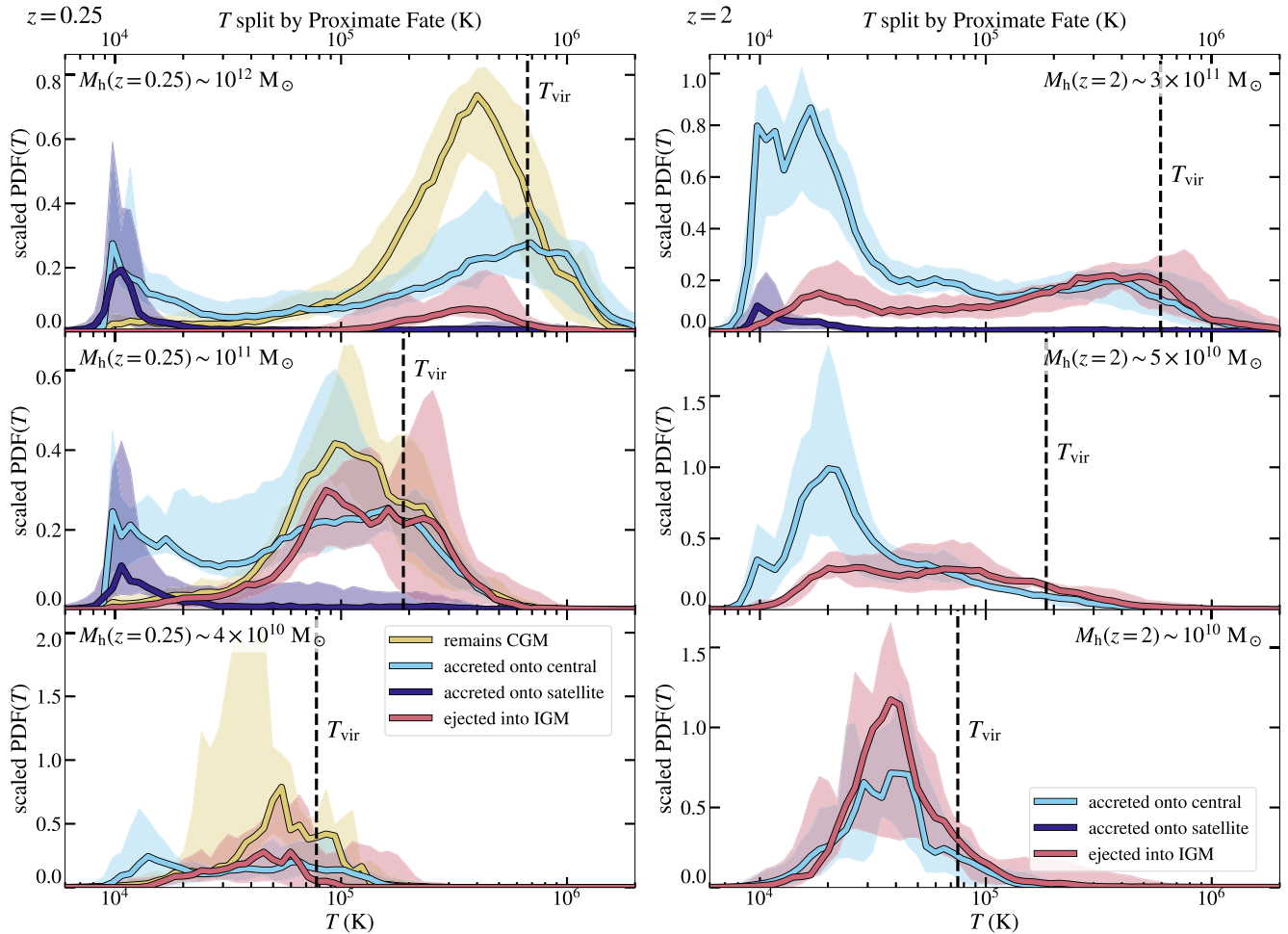


Figure 7. The temperature distribution of CGM gas for different proximate fates at $z = 0.25$ (left) and $z = 2$ (right). In each panel, the temperature distributions are weighted by the contributions of the different fates to the total CGM mass. The top, middle, and bottom panels correspond to haloes with $M_h(z = 0) \sim 10^{12,11,10} M_\odot$, respectively. The solid lines indicate the median value for the temperature bin across different haloes, while the shaded region encompasses the 16th–84th percentiles. The vertical dashed lines indicate halo virial temperatures.

cool gas observed in the CGM of haloes in the parameter space covered by our analysis is likely to next accrete on to a galaxy (except perhaps for the low-mass progenitors of $\sim 10^{10} M_\odot$ at $z = 2$, which eject a lot of mass into the IGM). Previous cosmological simulations also find that a large fraction of the cool CGM gas will accrete on to galaxies (e.g. Ford et al. 2014). Interestingly, for $10^{12} M_\odot$ haloes at $z = 0.25$, about half of the cool CGM with $T \approx 10^4$ K will next accrete on to satellite galaxies. As we will discuss further in Section 3.4, this is because cool gas in hot haloes in our simulations is strongly associated with non-linear structures, in particular satellite winds that recycle. This is especially so at larger halo radii, where satellite wind is more prevalent than wind from the central galaxy (H19, Fig. 14).

3.3.3 Fates by metallicity

As demonstrated explicitly in H19, the metallicity of CGM gas is a strong function of its origin (i.e. as galactic winds versus IGM accretion) and the host halo mass. In this section we investigate the connection between metallicity and the proximate fate of CGM gas. Fig. 8 shows the metallicity distributions of CGM gas, with solid (dashed) lines indicating the median between haloes in a given

halo mass bin for simulations run without (with) turbulent metal diffusion. The distributions are normalized by contribution to the total CGM mass, as we normalized the temperature distributions in the previous section. We use the same value of the solar metallicity as used in H19, $Z_\odot = 0.0134$ (Asplund et al. 2009). Note that our simulations have a metallicity floor at $Z \approx 10^{-4} Z_\odot$. To account for a spike in the values of the PDF near the metallicity floor, we expand the bottom-most histogram bin to cover $Z = 10^{-4} - 10^{-3.5} Z_\odot$.

Fig. 8 shows that, for a given halo mass bin and redshift, the CGM metallicity distributions of different proximate fates are broad and overlap substantially. As a result, the simulations indicate that we cannot in general use the metallicity of a CGM absorber to reliably predict whether the gas will next accrete on to galaxy, be ejected into the IGM, or remain in the CGM. We note, however, that while metallicity distributions of different proximate fates overlap broadly, the median metallicity for different proximate fates can differ significantly. For example, at $z = 0.25$ the median metallicity of gas that will accrete on to galaxies is ~ 1 dex higher than the metallicity of gas that will remain in the CGM until $z = 0$.

The results for simulations including a subgrid model turbulent metal diffusion (see Section 2.1) are shown by dashed lines in Fig. 8. In these simulations, low-metallicity gas particles gain

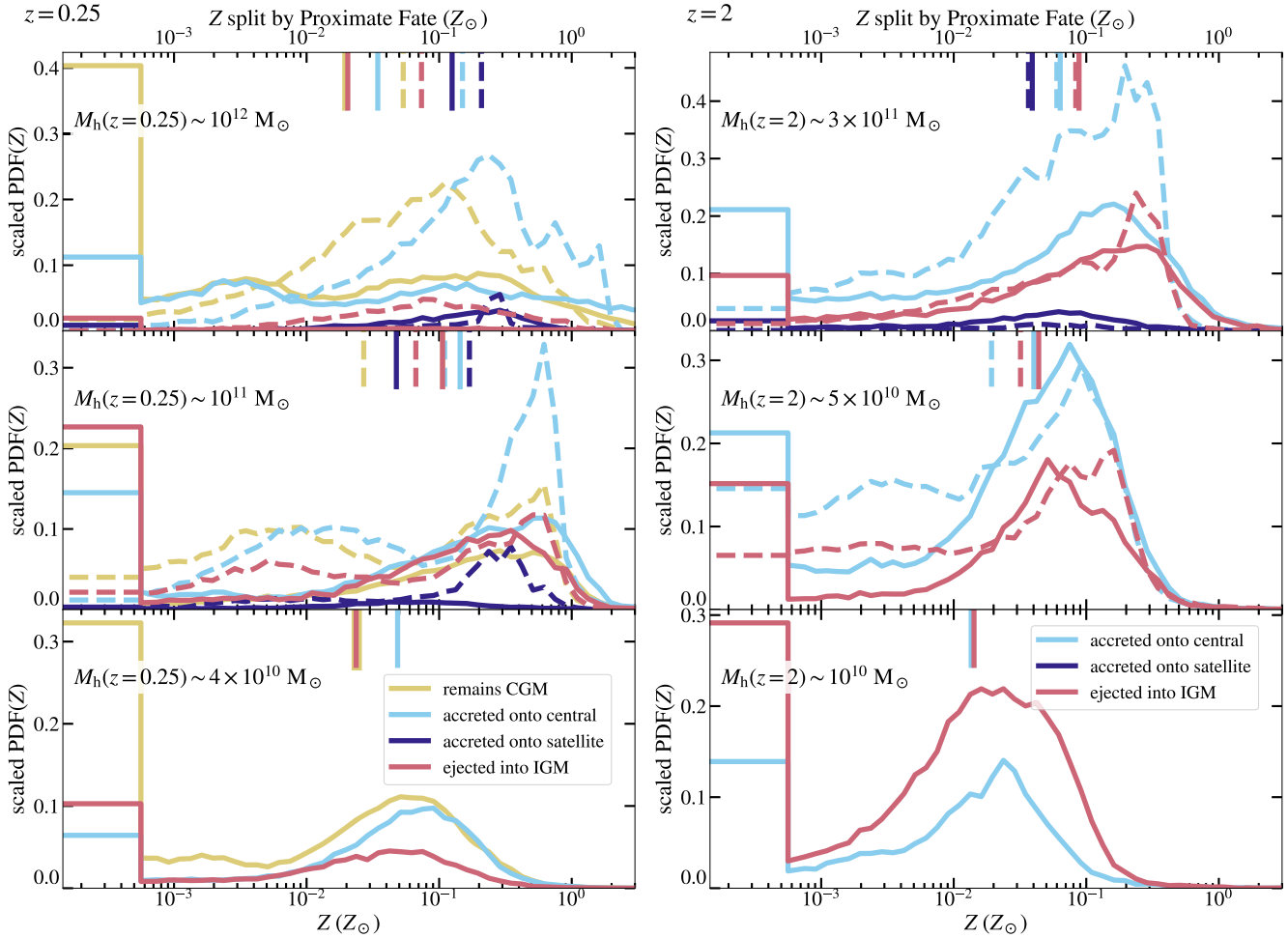


Figure 8. The metallicity distribution of CGM gas with a given proximate fate weighted by the contribution of such gas to the total CGM mass. The solid (dashed) lines indicate the median value of the distribution across all simulations in that mass bin run without (with) a prescription for subgrid turbulent diffusion. The median metallicities are indicated on the top axis with short vertical segments. While the distributions change for simulations with/without metal diffusion, for both types of simulations and at both $z = 0.25$ and 2 the metallicity distributions of different fates overlap strongly, indicating that the metallicity of CGM gas elements is not a reliable indicator of its fate. While the distributions overlap strongly, at $z = 0.25$ the median metallicity of gas accreted on to galaxies can be up to ~ 1 dex higher than the median metallicity of gas that will remain in the CGM or be ejected into the IGM by $z = 0$.

metals through contact with higher metallicity gas. Subgrid metal diffusion can significantly boost the metallicity of otherwise metal-poor gas. As can be seen in Fig. 8, this almost entirely suppresses the metallicity floor peaks for the CGM of all possible fates. However, since metallicity distributions for different proximate fates nevertheless overlap strongly, subgrid metal diffusion does not affect our qualitative conclusion that metallicity is not in general a robust predictor of the fate of a CGM gas element.

The inner CGM and outer CGM typically probe very different physical regimes: Wind from the central galaxy can provide up to ~ 80 per cent of the mass in the inner CGM while IGM accretion can provide a similar fraction of the CGM mass at $R \sim R_{\text{vir}}$ (H19). We analysed the metallicity distributions of proximate fates as a function of radius and found strong overlap between the metallicity distributions at all radii, qualitatively similar to the results in Fig. 8.

3.4 Connection between origin and fate

In this section, we study the relationship between the proximate fate and the origin of CGM gas. Fig. 9 shows CGM mass fractions at

$z = 0.25$ and 2 for gas that has both a given proximate fate *and* a given origin, as defined in H19. Briefly, *IGM accretion* is gas that has arrived in the CGM without spending $t > 30$ Myr in any galaxy; *wind* is gas that was ejected from the central galaxy; and *satellite wind* is gas that was ejected from a galaxy other than the central galaxy. The different panels correspond to different proximate fates and the different colours correspond to different origins. For example, the green data in the top left panel represent the fraction of total CGM mass that was ejected from the central galaxy and which will next accrete on to the central galaxy, i.e. a measure of the fraction of CGM mass from wind gas in the process of recycling. Comparing the relative values in a single panel provides insight into the origins of a given proximate fate, and comparing the relative values of the same colours across different panels provides insight into the fates of CGM gas of a given origin.

For most proximate fates, the most common origin is IGM accretion, in agreement with the results of H19 for the overall build-up of the CGM. The most striking exception is for the origin of CGM gas that next accretes on to satellites, especially for $10^{11} M_{\odot}$ and $10^{12} M_{\odot}$ progenitor haloes in the $z = 0.25$ column in Fig. 9. In this case, our analysis shows that the dom-

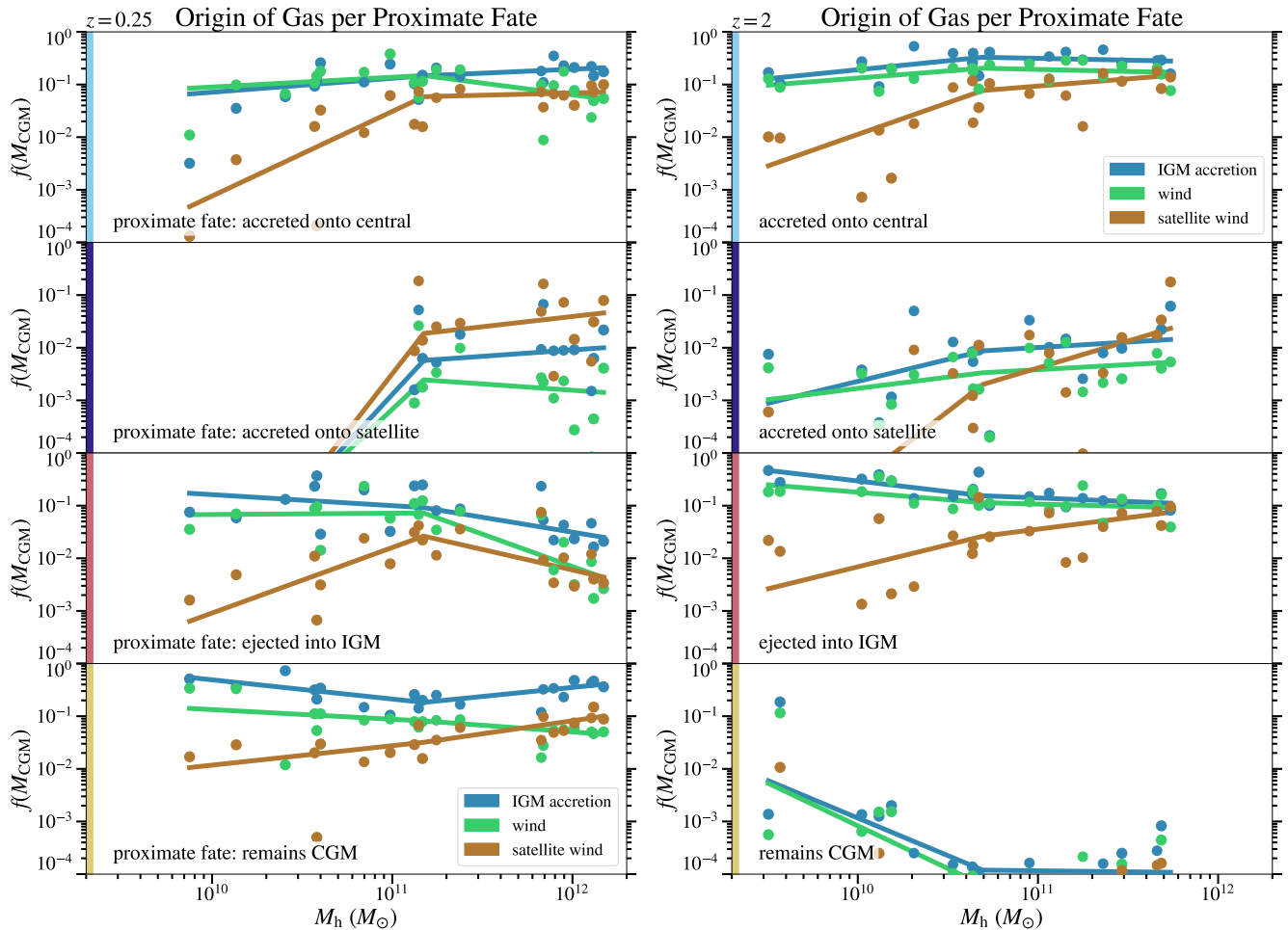


Figure 9. Connection between CGM origins and proximate fates. Different panels correspond to different proximate fates, and different colours within each panel correspond to different origins defined in Hafen et al. (2019). The coloured bands on the left show the colours used for proximate fates throughout the paper. Each point shows the CGM origin mass fraction at $z = 0.25$ (left) and $z = 2$ (right). Comparing the relative values for different colours in a single panel indicates the origin of CGM mass for a given proximate fate. Comparing the relative values of the same colour across different panels indicates the relative prevalence of proximate fates for a given origin. For most proximate fates, the most common origin is IGM accretion, in agreement with the overall build-up of the CGM (see H19). The most striking exception is that, at the high-mass end and especially at $z = 0.25$, the dominant origin for CGM that next accretes on to satellites is satellite wind. This reflects the importance of wind recycling around satellites.

inant origin is satellite wind. In other words, most of the CGM that next accretes on to satellite galaxies is recycling satellite wind.⁷

Fig. 9 also contains an interesting result concerning the mass loading of galactic winds as they expand in the CGM. The third row reveals that CGM gas that will be ejected into the IGM is primarily of IGM accretion origin, not directly from galactic winds. This indicates that winds driven by the central galaxy are significantly mass loaded in the CGM before reaching $\sim R_{\text{vir}}$, echoing previous results from FIRE-1 simulations from Muratov et al. (2017). The effective mass loading factor in the CGM can actually be larger than suggested by this result, since much of the CGM swept up by fresh galactic winds can be ‘ancient winds’, i.e. CGM that would appear to be of wind origin in the figure.

⁷Movies for FIRE-2 simulations available at <http://tapir.caltech.edu/~sheagk/gasvids.html> illustrate this phenomenon.

4 DISCUSSION

4.1 Connections to previous work

One of the most direct comparisons we can make is to Ford et al. (2014), who also studied the origins and fates of CGM gas via a particle tracking analysis of smoothed particle hydrodynamics (SPH) cosmological simulations. In H19 we discussed the extent to which the origins of CGM gas matched with those calculated by Ford et al. (2014), finding broadly consistent results despite significant differences in the simulations. Because Ford et al. focus primarily on differentiating when gas is inside/outside a galaxy, our comparison is limited to comparing the fraction of CGM gas that is accreted on to either the central galaxy or a satellite galaxy. For haloes with $M_h < 10^{11.5} M_\odot$ at $z = 0.25$, Ford et al. found that ~ 40 per cent of the CGM gas accretes on to a galaxy, compared to ~ 30 per cent of the CGM gas that accretes at least once between between $z = 0.25$ and 0 at $M_h \sim 10^{11} M_\odot$ in our simulation (see proximate fates in Section 6). On the other hand, for haloes with $M_h > 10^{11.5} M_\odot$ at $z = 0.25$ Ford et al. found that only

~ 7 per cent of the CGM gas accretes on to a galaxy, compared to up to ~ 40 per cent for some of our $M_h \sim 10^{12} M_\odot$ haloes. While our values for lower mass haloes are in broad agreement, the difference in CGM accretion for higher mass haloes is possibly a result of differences in feedback models. Another potentially important difference is that the simulations analysed in Ford et al. (2014) were produced with a ‘traditional’ SPH solver, and as such have suppressed cooling relative to simulations produced using hydrodynamic solvers with improved shock capturing and treatment of subsonic turbulence (e.g. Kereš et al. 2012; Hopkins et al. 2018).

Tollet et al. (2019) studied the baryon cycle of galaxies and haloes in the NIHAO suite of ~ 90 zoom-in simulations. On average, the NIHAO haloes and galaxies retain a fraction of their baryon budget similar to the FIRE-2 simulations (the baryon fractions in FIRE-2 haloes are analysed in H19). Tollet et al. (2019) calculate for a given halo the fraction of the total baryonic mass accumulated over the life of the universe that is no longer inside the halo at $z = 0$, and find values ranging over ~ 0.2 – 0.6 . This quantity relates to but is different from the quantities we calculate. Our Figs 2 and 6 are closest, and contain information on the fraction of CGM mass (as opposed to total halo mass) at a given redshift (as opposed to being summed across all redshifts) that is found outside the halo at $z = 0$. For gas found in the CGM at $z = 0.25$, we find that at most ~ 40 per cent of the CGM mass is found in the IGM at $z = 0$, and in most cases much less. For gas that will be in the CGM at $z = 2$, we find a significantly higher fraction of mass found outside the CGM by $z = 0$ (up to ~ 80 per cent), more consistent with the values identified by Tollet et al.; Tollet et al. (2019) also briefly discuss the fraction of ejected material that originates as wind from satellite galaxies, and conclude that of the ejected material satellite winds only provide a small fraction, which we demonstrate explicitly is the case in our simulations (Fig. 9).

We connect our results to the galaxy-centric baryon cycle by comparing to the analysis of Anglés-Alcázar et al. (2017), who studied the origin of baryonic mass in central galaxies using a suite of six FIRE-1 simulations spanning $M_h(z = 0) \sim 10^{10}$ – $10^{13} M_\odot$. Among other results, Anglés-Alcázar et al. find that the contribution of intergalactic transfer (satellite wind that is accreted on to the central galaxy) to galactic baryons increases with increasing halo masses. We find a similar trend in the increase in satellite wind in the CGM that accretes on to the central galaxy with increasing halo mass in Fig. 9. For $10^{12} M_\odot$ progenitors, the contribution of satellite wind to galactic accretion can exceed the contribution of central wind, at both $z = 0.25$ and 2. Anglés-Alcázar et al. (2017) argued based on visualizations that satellites experience multiple bursts of star formation as they orbit a central galaxy, driving winds that can either accrete on to the central galaxy or recycle on to the satellite. Our results are consistent with this interpretation, and quantitatively demonstrate that at $z = 0.25$ a comparable amount of satellite wind accretes on to the central galaxy, recycles on to satellite, and remains in the CGM (as seen by comparing the orange points in the first and second rows of the left side of Fig. 9). We emphasize that accretion on to satellites is dominated by satellite wind, as opposed to gas from other origins. However, a small fraction of the gas that accretes on to satellite galaxies is intergalactic transfer: wind ejected from the central galaxy that accretes on to satellite galaxies. Observations of metal-enriched satellite galaxies may be observational evidence of this channel of the baryon cycle (Schaefer et al. 2019). Both of these channels of the baryon cycle are related to the inter-Lagrangian transfer of gas quantified by Borrow, Anglés-Alcázar & Davé (2020) using the SIMBA simulations (Davé et al. 2019), corresponding to the transfer of baryons from one dark matter halo Lagrangian

region in the universe to another due to hydrodynamic and feedback processes.

It is useful to connect gas accretion on to satellites to star formation in satellites. Garrison-Kimmel et al. (2019) use FIRE-2 simulations to study the star formation history of dwarf galaxies and find that satellites have a lower star formation rate than isolated galaxies, consistent with a number of observations (e.g. Baldry et al. 2006; Kimm et al. 2009; Wang et al. 2014). The star formation histories presented in Garrison-Kimmel et al. (2019) are broadly consistent with observations of satellite galaxies in the Local Group (Weisz et al. 2014; Skillman et al. 2017). Satellite galaxy quenching is likely related to interactions with the host halo stripping satellite ISM, a process that can be accentuated by the ejection of winds from satellites that are then more easily stripped (e.g. Bustard et al. 2018). However, satellite galaxy quenching is not necessarily immediate or complete: Garrison-Kimmel et al. find median quenching times $\gtrsim 1$ Gyr, with many $M_* \gtrsim 10^7 M_\odot$ galaxies forming stars until $z = 0$, consistent with observationally derived satellite quenching time-scales at this mass (e.g. Fillingham et al. 2015; Wetzel, Tollerud & Weisz 2015). This continued star formation may be fuelled by accretion of gas from the CGM. Of the gas in the CGM at a *single* redshift (either $z = 0$ or 2 in our work), a gas mass greater than or equal to the total ISM mass of all satellites will accrete on to satellites (Fig. 6 shows the fraction of CGM gas accreted on to satellites, while fig. 9 in H19 shows the fraction of CGM gas currently in satellite ISM). Gas that is in the CGM at other redshifts may also accrete on to satellite galaxies, making this a lower limit on the mass of gas accreted on to satellites.

4.2 Implications for observations

Our simulations that predict $\gtrsim 30$ per cent of the $z = 2$ CGM mass will be ejected from the halo (R_{vir}) across all analysed halo masses, while at $z = 0.25$ the CGM mass fractions that will be ejected into the IGM by $z = 0$ peak at a median ~ 10 per cent for $10^{11} M_\odot$ haloes (Fig. 6) and are typically only a few per cent for $10^{12} M_\odot$ haloes. These results are consistent with observed CGM kinematics. At $z \sim 2$, Rudie et al. (2019) measured the line-of-sight velocity for absorption systems around $10^{12} M_\odot$ haloes. In five of the seven galaxies with detected metal lines within the projected virial radius, Rudie et al. find at least some absorption systems with centroid line-of-sight velocities that exceed the escape velocity of the halo. Rudie et al. note that these absorbers could arise from a source outside the CGM of the central galaxy, but argue that given the number of detections it is likely that at least some of the apparently unbound absorbers are associated with the CGM. At $z < 1$, absorption systems that probe the CGM in haloes with $M_h \gtrsim 10^{12} M_\odot$ instead usually have line-of-sight velocities below the escape speed (e.g. Tumlinson et al. 2011; Stocke et al. 2013; Borthakur et al. 2016), consistent with much lower CGM fractions of gas ejected from our simulated $z = 0.25 L^*$ haloes. Moreover, Borthakur et al. (2016) find that CGM absorbers in low-redshift $\sim 10^{11} M_\odot$ haloes more frequently have line-of-sight velocities exceeding the escape velocity, similar to the increased fraction of ejected CGM gas for the simulated $10^{11} M_\odot$ progenitors.

Identifying accretion on to galaxies has long been a goal of observational studies of the CGM (for a review, see Fox & Davé 2017). We find that $\gtrsim 80$ per cent of gas with $T < 10^{4.7}$ K will accrete on to a central or satellite galaxy, for haloes with $M_h \gtrsim 10^{11} M_\odot$ at both $z = 0.25$ and 2 (Fig. 7). Our results thus suggest that observations of low-ionization absorption systems typically probe gas that will accrete on to a galaxy, regardless of the metal content of the absorption system (which does not uniquely determine fate; Fig. 8). In $10^{12} M_\odot$

haloes at $z \sim 0$, however, this channel is subdominant to accretion of hot gas (Section 3.3.2).

5 CONCLUSIONS

We used FIRE-2 cosmological zoom-in simulations to study the fates of gas found in the $z = 0.25$ and 2 CGM of haloes in the mass range $M_h(z=0) \sim 10^{10}$ – $10^{12} M_\odot$. As with our analysis of the origins of the CGM (H19), we followed the full histories of individual gas elements through the duration of the simulations. Using the particle trajectories, we classified gas particles according to their proximate fate upon leaving the CGM (i.e. accretion on to the central galaxy, accretion on to a satellite galaxy, ejection into the IGM, or particles that never leave the CGM) as well as their ultimate fate (the component of the baryon cycle they reside in at $z = 0$). Our main results are as follows:

(i) For haloes with $M_h(z=0) \sim 10^{10}$ – $10^{12} M_\odot$, half the $z = 0.25$ CGM mass will move out of the CGM by $z = 0$ (i.e. after 3 Gyr), while at $z = 2$ half the mass that comprises the CGM will move out of the CGM in $\lesssim 1$ Gyr (Fig. 2). For haloes with $M_h \gtrsim 5 \times 10^{10} M_\odot$, the time for half the mass (tracking fixed gas elements) to move in and out of the CGM is largely independent of halo mass and scales roughly with the halo dynamical time, but with high halo-to-halo variability (Fig. 3). For lower mass haloes, the CGM can consist of largely the same gas for multiple Gyr owing to support by heating from the cosmic UV background.

(ii) Of the CGM at $z = 2$, about half ends up as central galaxy baryons (either ISM or stars) by $z = 0$ in $M_h(z=2) \sim 5 \times 10^{11} M_\odot$ haloes, but most of the CGM in lower mass haloes is ejected into the IGM. On the other hand, most of the CGM mass at $z = 0.25$ remains in the CGM by $z = 0$ at all halo masses analysed.

(iii) Proximate and ultimate fates are in general different because of the complex cycling of gas through galaxies and the CGM. For example, while most of the CGM in $M_h(z=2) \sim 5 \times 10^{10} M_\odot$ haloes is ultimately ejected into the IGM, most of it first accretes on to the central galaxy before ultimate ejection.

(iv) Ejection of CGM gas into the IGM depends strongly on redshift and halo mass. At $z = 2$, when star formation is vigorous and outflows are powerful in the haloes analysed, up to ~ 80 per cent of the CGM mass is ejected into the IGM by $z = 0$, especially in lower mass haloes. On the other hand, the $z = 0.25$ CGM mass fractions that will be ejected into the IGM by $z = 0$ peak at a median ~ 10 per cent for $10^{11} M_\odot$ haloes and are typically only a few per cent for $10^{12} M_\odot$ haloes. These trends are qualitatively consistent with observed CGM kinematics relative to inferred halo escape velocities.

(v) Of the CGM gas that subsequently accretes on to the central galaxy in the progenitors of $M_h(z=0) \sim 10^{12} M_\odot$ haloes, most of it is cool ($T \sim 10^4$ K) at $z = 2$ but hot ($\sim T_{\text{vir}}$) at $z \sim 0.25$. This is consistent with transition from cold mode to hot mode accretion expected at this mass scale.

(vi) For $M_h(z=0) \gtrsim 10^{11} M_\odot$ haloes ~ 80 per cent of the cool/cold ($T < 10^{4.7}$ K) CGM gas will accrete on to either the central galaxy or a satellite galaxy upon leaving the CGM. This suggests that low-ionization absorption systems are likely to probe accreting gas.

(vii) Metals have similar proximate fates as those of baryons overall, though metal-rich CGM gas is more likely to accrete on to central galaxies at $z = 0.25$ (Fig. 6). Since the majority of the metals are injected into the CGM by winds from central galaxies (H19), this trend reflects the efficiency of wind recycling around low-redshift galaxies.

(viii) The metallicity distributions of different fates overlap strongly, making it challenging to use observationally inferred metallicities alone to predict the fate of absorption systems. Despite the substantial overlap in distributions, the median metallicity of different fates can differ by up to ~ 1 dex.

(ix) The majority of gas ejected from the CGM into the IGM is pristine gas that has never entered a galaxy (Fig. 9). This is because winds from galaxies sweep up a large amount of CGM gas as they travel to R_{vir} and the total CGM mass is generally dominated by IGM accretion (H19).

(x) In addition to wind recycling around central galaxies, satellite galaxies undergo frequent satellite wind recycling, even as they pass through a more massive halo (Fig. 9). Gas that accretes on to satellite galaxies can provide up to ~ 10 per cent of the total CGM mass for $z = 0.25 L^*$ haloes (Fig. 6), and is roughly half of the $T \sim 10^4$ K gas in these haloes (Fig. 7).

Overall, our particle tracking analysis demonstrates that while the CGM is affected by a complex interplay of forces and thermodynamic processes, analysing the CGM from the perspective of fates (and origins) produces a number of important insights. These insights are useful both for our understanding of the complex simulation results and to develop a holistic framework for the interpretation of CGM observations. Processed data to generate the majority of the figures in this paper are available online.⁸

ACKNOWLEDGEMENTS

We thank Robert Feldmann, Alex Gurvich, Sarah Wellons, Luke Zoltan Kelley, Andrey Kravtsov, and Nick Gnedin for useful discussions. We thank Alex Gurvich for help integrating FIREFLY into our analysis. ZH was supported by the National Science Foundation under grant DGE-0948017. CAFG was supported by the National Science Foundation through grants AST-1412836, AST-1517491, AST-1715216, and CAREER award AST-1652522, by NASA through grants NNX15AB22G and 17-ATP17-0067, by the Space Telescope Science Institute through grants *HST*-GO-14681.011, *HST*-GO-14268.022-A, and *HST*-AR-14293.001-A, and by a Cottrell Scholar Award from the Research Corporation for Science Advancement. The Flatiron Institute is supported by the Simons Foundation. JS is supported as a Center for Interdisciplinary Exploration and Research in Astrophysics (CIERA) Fellow by the CIERA Postdoctoral Fellowship Programme at Northwestern University. DK and TKC were supported by National Science Foundation grant AST-1715101 and by a Cottrell Scholar Award from the Research Corporation for Science Advancement. AW received support from NASA, through ATP grant 80NSSC18K1097 and *HST* grants GO-14734 and AR-15057 from STScI, a Hellman Fellowship from UC Davis, and the Heising-Simons Foundation. KE was supported by an NSF Graduate Research Fellowship. NM acknowledges the support of the Natural Sciences and Engineering Research Council of Canada (NSERC). This research was undertaken, in part, thanks to funding from the Canada Research Chairs programme. Numerical calculations were run on the Quest computing cluster at Northwestern University, the Wheeler computing cluster at Caltech, XSEDE allocations TG-AST130039 and TG-AST120025, Blue Waters PRAC allocation NSF.1713353, and NASA HEC allocation SMD-16-7592.

⁸https://github.com/zhafen/CGM_fate_analysis

REFERENCES

- Adelberger K. L., Steidel C. C., Pettini M., Shapley A. E., Reddy N. A., Erb D. K., 2005, *ApJ*, 619, 697
- Anglés-Alcázar D., Faucher-Giguère C.-A., Kereš D., Hopkins P. F., Quataert E., Murray N., 2017, *MNRAS*, 470, 4698
- Asplund M., Grevesse N., Sauval A. J., Scott P., 2009, *ARA&A*, 47, 481
- Baldry I. K., Balogh M. L., Bower R. G., Glazebrook K., Nichol R. C., Bamford S. P., Budavari T., 2006, *MNRAS*, 373, 469
- Behroozi P. S., Wechsler R. H., Conroy C., 2013, *ApJ*, 770, 57
- Birnboim Y., Dekel A., 2003, *MNRAS*, 345, 349
- Bordoloi R. et al., 2014, *ApJ*, 796, 136
- Borrow J., Anglés-Alcázar D., Davé R., 2020, *MNRAS*, 491, 6102
- Borthakur S. et al., 2016, *ApJ*, 833, 259
- Bouché N., Murphy M. T., Kacprzak G. G., Péroux C., Contini T., Martin C. L., Dessauges-Zavadsky M., 2013, *Science*, 341, 50
- Bryan G. L., Norman M. L., 1998, *ApJ*, 495, 80
- Burchett J. N. et al., 2019, *ApJ*, 877, L20
- Bustard C., Pardy S. A., D’Onghia E., Zweibel E. G., Gallagher J. S., 2018, *ApJ*, 863, 49
- Chen H.-W., Zahedy F. S., Johnson S. D., Pierce R. M., Huang Y.-H., Weiner B. J., Gauthier J.-R., 2018, *MNRAS*, 479, 2547
- Christensen C. R., Davé R., Brooks A., Quinn T., Shen S., 2018, *ApJ*, 867, 142
- Davé R., Oppenheimer B. D., Finlator K., 2011, *MNRAS*, 415, 11
- Davé R., Anglés-Alcázar D., Narayanan D., Li Q., Rafieferantsoa M. H., Appleby S., 2019, *MNRAS*, 486, 2827
- Dekel A., Birnboim Y., 2006, *MNRAS*, 368, 2
- El-Badry K. et al., 2018, *MNRAS*, 473, 1930
- Escala I. et al., 2018, *MNRAS*, 474, 2194
- Fang T., Buote D., Bullock J., Ma R., 2015, *ApJS*, 217, 21
- Faucher-Giguère C. A., Lidz A., Zaldarriaga M., Hernquist L., 2009, *ApJ*, 703, 1416
- Faucher-Giguère C.-A., Hopkins P. F., Kereš D., Muratov A. L., Quataert E., Murray N., 2015, *MNRAS*, 449, 987
- Faucher-Giguère C.-A., Feldmann R., Quataert E., Kereš D., Hopkins P. F., Murray N., 2016, *MNRAS*, 461, L32
- Faucher-Giguère C. A., Kereš D., Ma C. P., 2011, *MNRAS*, 417, 2982
- Fielding D., Quataert E., McCourt M., Thompson T. A., 2017, *MNRAS*, 466, 3810
- Fillingham S. P., Cooper M. C., Wheeler C., Garrison-Kimmel S., Boylan-Kolchin M., Bullock J. S., 2015, *MNRAS*, 454, 2039
- Ford A. B., Oppenheimer B. D., Davé R., Katz N., Kollmeier J. A., Weinberg D. H., 2013, *MNRAS*, 432, 89
- Ford A. B., Davé R., Oppenheimer B. D., Katz N., Kollmeier J. A., Thompson R., Weinberg D. H., 2014, *MNRAS*, 444, 1260
- Fox A., Davé R., eds, 2017, *Astrophysics and Space Science Library*, Vol. 430, Gas Accretion on to Galaxies. Springer Int. Publ., Cham
- Garrison-Kimmel S. et al., 2019, *MNRAS*, 15, 1
- Gill S. P. D., Knebe A., Gibson B. K., 2004, *MNRAS*, 351, 399
- Gupta A., Mathur S., Krongold Y., Nicastro F., Galeazzi M., 2012, *ApJ*, 756, 4
- Hafen Z. et al., 2017, *MNRAS*, 469, 2292
- Hafen Z. et al., 2019, preprint ([arXiv:1910.01123](https://arxiv.org/abs/1910.01123)) (H19)
- Henley D. B., Shelton R. L., 2010, *ApJS*, 187, 388
- Henley D. B., Shelton R. L., Kwak K., Joung M. R., Mac Low M. M., 2010, *ApJ*, 723, 935
- Ho S. H., Martin C. L., Turner M. L., 2019, *ApJ*, 875, 1
- Hopkins P. F., 2015, *MNRAS*, 450, 53
- Hopkins P. F., 2017, *MNRAS*, 466, 3387
- Hopkins P. F., Kereš D., Onorbe J., Faucher-Giguère C.-A., Quataert E., Murray N., Bullock J. S., 2014, *MNRAS*, 445, 581
- Hopkins P. F. et al., 2018, *MNRAS*, 480, 800
- Hummels C. B., Bryan G. L., Smith B. D., Turk M. J., 2013, *MNRAS*, 430, 1548
- Ji S. et al., 2019, preprint ([arXiv:1909.00003](https://arxiv.org/abs/1909.00003))
- Johnson S. D., Chen H.-W., Mulchaey J. S., 2015, *MNRAS*, 449, 3263
- Johnson S. D., Chen H.-W., Mulchaey J. S., Schaye J., Straka L. A., 2017, *ApJ*, 850, L10
- Keeney B. A. et al., 2017, *ApJS*, 230, 6
- Kereš D., Katz N., Weinberg D. H., Davé R., 2005, *MNRAS*, 363, 2
- Kereš D., Katz N., Davé R., Fardal M., Weinberg D. H., 2009, *MNRAS*, 396, 2332
- Kereš D., Vogelsberger M., Sijacki D., Springel V., Hernquist L., 2012, *MNRAS*, 425, 2027
- Kimm T. et al., 2009, *MNRAS*, 394, 1131
- Knollmann S. R., Knebe A., 2009, *ApJS*, 182, 608
- Kroupa P., 2001, *MNRAS*, 322, 231
- Leitherer C. et al., 1999, *ApJS*, 123, 3
- Liang C. J., Chen H.-W., 2014, *MNRAS*, 445, 2061
- McQuinn M., Werk J. K., 2018, *ApJ*, 852, 33
- Martin C. L., 2005, *ApJ*, 621, 227
- Mathews W. G., Prochaska J. X., 2017, *ApJ*, 846, L24
- Moster B. P., Naab T., White S. D., 2013, *MNRAS*, 428, 3121
- Muratov A. L., Kereš D., Faucher-Giguère C.-A., Hopkins P. F., Quataert E., Murray N., 2015, *MNRAS*, 454, 2691
- Muratov A. L. et al., 2017, *MNRAS*, 468, 4170
- Nelson D., Vogelsberger M., Genel S., Sijacki D., Kereš D., Springel V., Hernquist L., 2013, *MNRAS*, 429, 3353
- Oppenheimer B. D., Davé R., Kereš D., Fardal M., Katz N., Kollmeier J. A., Weinberg D. H., 2010, *MNRAS*, 406, 2325
- Planck Collaboration VI, 2018, preprint ([arXiv:1807.06209](https://arxiv.org/abs/1807.06209))
- Prochaska J. X., Wolfe A. M., 2009, *ApJ*, 696, 1543
- Prochaska J. X., Hennawi J. F., Simcoe R. A., 2013, *ApJ*, 762, L19
- Putman M., Peek J., Joung M., 2012, *ARA&A*, 50, 491
- Rubin K. H. R., Prochaska J. X., Koo D. C., Phillips A. C., Martin C. L., Winstrom L. O., 2014, *ApJ*, 794, 156
- Rudie G. C. et al., 2012, *ApJ*, 750, 67
- Rudie G. C., Steidel C. C., Pettini M., Trainor R. F., Strom A. L., Hummels C. B., Reddy N. A., Shapley A. E., 2019, preprint ([arXiv:1903.00004](https://arxiv.org/abs/1903.00004))
- Schaefer A. L. et al., 2019, *ApJ*, 884, 1
- Skillman E. D. et al., 2017, *ApJ*, 837, 102
- Sravan N. et al., 2016, *MNRAS*, 463, 120
- Steidel C. C., Erb D. K., Shapley A. E., Pettini M., Reddy N., Bogosavljević M., Rudie G. C., Rakic O., 2010, *ApJ*, 717, 289
- Stern J., Faucher-Giguère C.-A., Hennawi J. F., Hafen Z., Johnson S. D., Fielding D., 2018, *ApJ*, 865, 91
- Stern J., Fielding D., Faucher-Giguère C.-A., Quataert E., 2019, *MNRAS*, 488, 2549
- Stern J., Fielding D., Faucher-Giguère C.-A., Quataert E., 2020, *MNRAS*, 492, 6042
- Stewart K. R. et al., 2017, *ApJ*, 843, 47
- Stocke J. T., Keeney B. A., Danforth C. W., Shull J. M., Froning C. S., Green J. C., Penton S. V., Savage B. D., 2013, *ApJ*, 763, 148
- Stocke J. T. et al., 2014, *ApJ*, 791, 128
- Tollet D., Cattaneo A., Macciò A. V., Dutton A. A., Kang X., 2019, *MNRAS*, 485, 2511
- Tumlinson J. et al., 2011, *Science*, 334, 948
- Tumlinson J., Peebles M. S., Werk J. K., 2017, *ARA&A*, 55, 389
- van de Voort F., Schaye J., Booth C. M., Dalla Vecchia C., 2011, *MNRAS*, 415, 2782
- van de Voort F., Quataert E., Hopkins P. F., Faucher-Giguère C.-A., Feldmann R., Kereš D., Chan T. K., Hafen Z., 2016, *MNRAS*, 463, 4533
- Veilleux S., Cecil G., Bland-Hawthorn J., 2005, *ARA&A*, 43, 769
- Wang W., Sales L. V., Henriques B. M. B., White S. D. M., 2014, *MNRAS*, 442, 1363
- Weisz D. R., Dolphin A. E., Skillman E. D., Holtzman J., Gilbert K. M., Dalcanton J. J., Williams B. F., 2014, *ApJ*, 789, 147
- Werk J. K., Prochaska J. X., Thom C., Tumlinson J., Tripp T. M., O’Meara J. M., Peebles M. S., 2013, *ApJS*, 204, 17
- Werk J. K. et al., 2014, *ApJ*, 792, 8
- Wetzel A. R., Tollerud E. J., Weisz D. R., 2015, *ApJ*, 808, L27
- Wiersma R. P. C., Schaye J., Theuns T., Dalla Vecchia C., Tornatore L., 2009, *MNRAS*, 399, 574

APPENDIX A: ADDITIONAL PATHLINE VISUALIZATIONS

In Section 3.2, we show radius versus time for gas particles in a few example cases at $z = 2$. Here we show the same results but for a characteristic $10^{11} M_{\odot}$ progenitor and a characteristic $10^{10} M_{\odot}$ progenitor (m10y). The CGM of $10^{11} M_{\odot}$ is dynamic, with gas recycling far into or ejected beyond the CGM at all redshifts. The CGM of $10^{10} M_{\odot}$ progenitors is typically more diffuse and long lived, with CGM gas often displaced by $\lesssim 20$ kpc over the course of $\gtrsim 5$ Gyr.

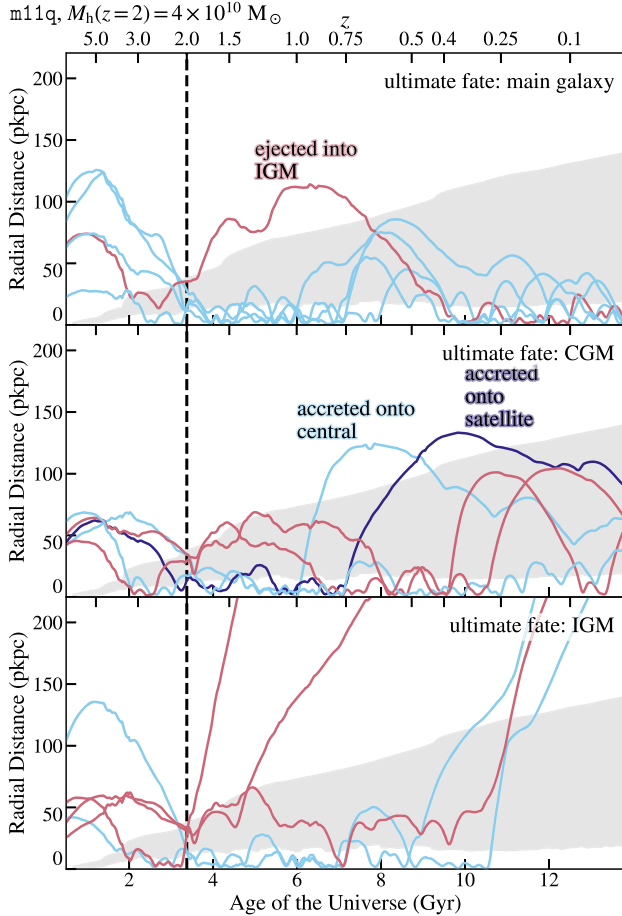


Figure A1. Same as Fig. 5, but for a representative $10^{11} M_{\odot}$ progenitor (m11q). Gas can be first lifted into the CGM, and then subsequently ejected into the IGM as part of a separate wind event.

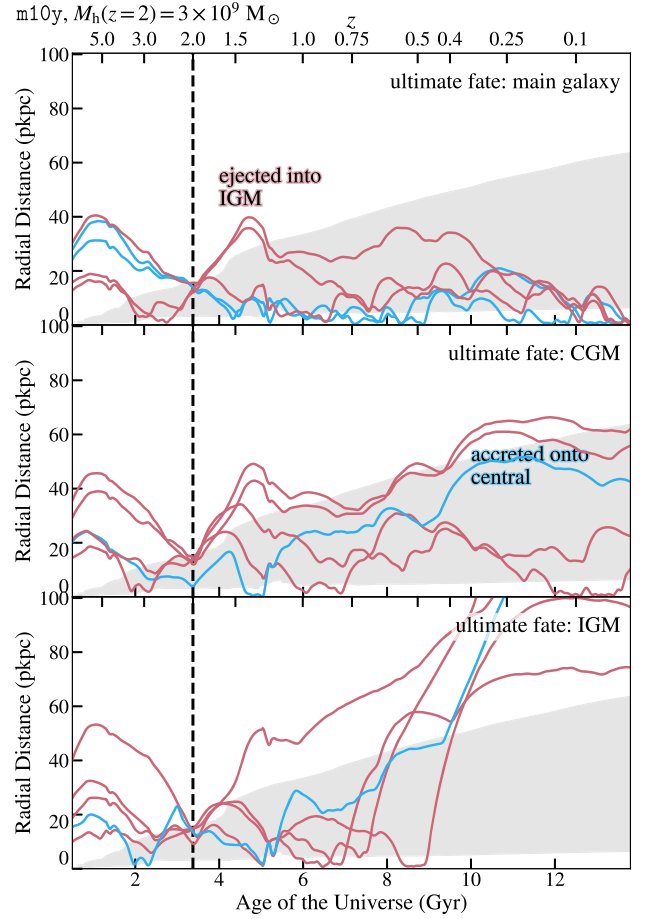


Figure A2. Same as Fig. 5, but for m10y. Gas in $M_h(z=0) \sim 10^{10} M_{\odot}$ progenitors typically moves a smaller radial distance over a given time, relative to the halo size, and is frequently buoyed via energy injection from winds.

This paper has been typeset from a $\text{\TeX}/\text{\LaTeX}$ file prepared by the author.